

Gate-Tunable Transmon Using Selective-Area-Grown Superconductor-Semiconductor Hybrid Structures on Silicon

Albert Hertel,^{1,*} Michaela Eichinger,^{1,†} Laurits O. Andersen,¹ David M. T. van Zanten,¹ Sangeeth Kallatt,¹ Pasquale Scarlino,² Anders Kringhøj,¹ José M. Chavez-Garcia,¹ Geoffrey C. Gardner,^{3,4} Sergei Gronin,^{3,4} Michael J. Manfra,^{3,4,5,6} András Gyenis,^{1,‡} Morten Kjaergaard,¹ Charles M. Marcus,¹ and Karl D. Petersson^{1,2}

¹*Center for Quantum Devices, Niels Bohr Institute, University of Copenhagen, 2100 Copenhagen, Denmark*

²*Microsoft Quantum Lab–Copenhagen, 2100 Copenhagen, Denmark*

³*Birck Nanotechnology Center, Purdue University, West Lafayette, Indiana 47907 USA*

⁴*Microsoft Quantum Lab–West Lafayette, West Lafayette, Indiana 47907 USA*

⁵*Department of Physics and Astronomy, Purdue University, West Lafayette, Indiana 47907 USA*

⁶*School of Materials Engineering, and School of Electrical and Computer Engineering, Purdue University, West Lafayette, Indiana 47907 USA*

(Dated: February 23, 2022)

We present a gate-voltage tunable transmon qubit (gatemon) based on planar InAs nanowires that are selectively grown on a high resistivity silicon substrate using III-V buffer layers. We show that low loss superconducting resonators with an internal quality of 2×10^5 can readily be realized using these substrates after the removal of buffer layers. We demonstrate coherent control and readout of a gatemon device with a relaxation time, $T_1 \approx 700$ ns, and dephasing times, $T_2^* \approx 20$ ns and $T_{2,\text{echo}} \approx 1.3 \mu\text{s}$. Further, we infer a high junction transparency of 0.4 – 0.9 from an analysis of the qubit anharmonicity.

I. INTRODUCTION

Superconducting qubit systems are one of the most promising approaches towards realizing a large scale fault tolerant quantum processor [1]. In recent years, a transmon variant that uses voltage-tunable superconductor-semiconductor hybrid Josephson junctions (JJs), the gatemon, has been developed [2, 3] and realized in several material systems such as vapor-liquid-solid (VLS) nanowires [2], two-dimensional electron gases (2DEG) [4] and graphene [5]. These junctions have an inherent non-sinusoidal current-phase relationship and could be used to create new building blocks for quantum computing or as a tool for condensed matter experiments based on cQED techniques [5–8]. Further, these qubits could be interfaced with low dissipation cryogenic CMOS control systems [9].

In this work, we demonstrate coherent operations of a gatemon qubit fabricated using a material system with selective-area-grown Al-InAs hybrid structures [10, 11] on a Si substrate that has planar III-V buffer layers (Si SAG). This material system has the potential to combine the individual advantages of previously demonstrated material systems [2, 4, 5, 12] for future gatemon devices. First, similar to 2DEG-based gatemons [4], the number of

JJs are relatively easy to scale as the Al-InAs nanowires are monolithically integrated into the substrate using deterministic lithographic patterning techniques. Second, the qubit capacitor, readout and control components can be fabricated directly on the high resistivity silicon substrate with low dielectric loss [13], similar to VLS-nanowire gatemons [2]. Similar experiments implemented on III-V substrates report a resonator quality factor of 6×10^4 [4] or lower [4, 14–16] and qubit relaxation times up to a few microseconds [4]. The main source of losses on III-V substrates can be explained by the piezoelectric photon-phonon coupling in these materials [14, 15].

In this study, we demonstrate that the material system can be used to make gatemons. We introduce the device design and show that high quality resonators can be fabricated with the material system after the removal of the buffer layers. Next we show gate tunable qubits and study the qubit anharmonicity, concluding a high junction transparency. Finally, we demonstrate coherent oscillations and extract qubit relaxation and dephasing times of a qubit device.

II. DEVICES

Figure 1a shows an optical micrograph of the gatemon device. The T-shaped qubit island is capacitively coupled to a quarter-wave coplanar waveguide cavity with resonance frequency $f_r \approx 6.6$ GHz and has a total charging energy $E_C/h \approx 225$ MHz extracted from finite-element simulations. All parts of the readout circuit such as the cavity, transmission line and the qubit island are fabricated on the high resistivity (111) Si substrate with

* Current address: Institute for Semiconductor Nanoelectronics, Peter Grünberg Institute 9, Forschungszentrum Jülich & Jülich-Aachen Research Alliance (JARA), Forschungszentrum Jülich and RWTH Aachen University, Germany; These two authors contributed equally.

† These two authors contributed equally.

‡ Current address: Department of Electrical, Computer & Energy Engineering, University of Colorado Boulder, CO 80309, USA.

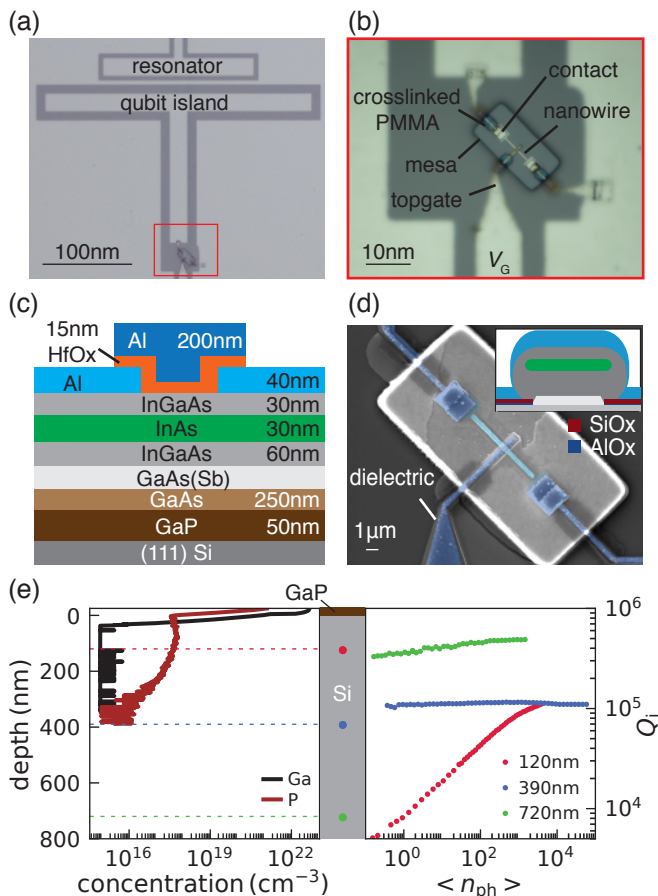


FIG. 1. **Qubit devices and microwave properties.** (a) Optical micrograph of the T-shaped qubit island that is capacitively coupled to a readout cavity. (b) Zoomed in optical micrograph of the junction region. The junction is positioned on a $\sim 1\mu\text{m}$ thick mesa. (c) Schematic of material stack around the junction. The InAs region (green) is proximitized by the epitaxial Al (light blue) and the junction is formed by selectively removing a short segment of the Al. (d) Scanning electron micrograph of the junction area. The mesa consists of GaAs, GaP and 400 nm of Si. The top gate metal climbs the mesa with the help of crosslinked PMMA. (inset) Cross section of the nanowire with the dielectric growth mask consisting of SiO_x and AlO_x. (e) (Left) Ga and P concentration of the material stack as a function of depth measured with secondary ion mass spectrometry. (Center) Schematic of the corresponding material stack. (Right). Internal quality factor of test resonators as a function of photon number for an etch depth into the Si of 120 nm (red), 390 nm (blue) and 720 nm (green).

a 4° miscut after etching the III-V layers. The qubit island is connected to the ground plane through a JJ that is located on a mesa with dimensions $10\mu\text{m} \times 20\mu\text{m}$ (Fig. 1b). The JJ is formed by selectively wet etching a $\sim 120\text{nm}$ long segment of the Al on the $\sim 300\text{nm}$ wide InAs SAG nanowire. The Josephson energy $E_J(V_G)$ of the junction is controlled by applying a gate voltage V_G via the Al top gate which is separated from the junction by 15 nm thick gate dielectric (HfO₂). The qubit frequency is given by $f_q \approx \sqrt{8E_J(V_G)E_C}/h$ in the transmon

limit ($E_J \gg E_C$) [17]. The top gate and Al wires that connect the nanowire with the ground plane and qubit island climb the mesa aided by layers of crosslinked poly-methyl methacrylate resist (PMMA). The primary purpose of the PMMA layers is to decouple the qubit from the lossy III-V material of the mesa. Figure 1c shows a schematic of the junction region of the heterostructure along the nanowire. A schematic cross section of the nanowire is shown in the inset of Fig. 1d. Further details of the material stack, including electrical transport characterization, are presented in Ref. [11] and briefly summarized here. The GaP/GaAs buffer is grown using metallic organic chemical vapor epitaxy and used to bridge the lattice mismatch between Si and InAs. Selective area growth [10] was used to grow planar InAs nanowires on the GaAs surface by molecular beam epitaxy [18]. To define the nanowire regions, thin films of AlO_x and SiO_x were deposited globally on the wafer and patterned using electron-beam lithography and a combination of reactive-ion etching (RIE) and wet etching techniques. Inside the mask opening the InAs nanowires were grown, where the Sb-dilute GaAs buffer and InGaAs layers are used to improve the InAs quality by promoting strain relaxation [10]. The top InGaAs layer is used to prevent surface damage of the InAs layer due to device processing. A blanket Al layer was deposited in-situ to ensure a high quality interface between the Al and semiconductor heterostructure [19, 20].

To fabricate qubit devices most of the epitaxial Al and dielectric growth mask were removed in a first step, followed by etching the GaAs/GaP buffer and $\sim 400\text{nm}$ of Si to define mesa structures. The removal of the top layers of Si are necessary for the fabrication of high quality resonators as will be discussed in Section III. A detailed summary of the device fabrication can be found in Appendix A.

III. MICROWAVE LOSS

Figure 1e (left panel) shows the doping profile of a Si substrate with GaP and GaAs grown on top of it measured by secondary ion mass spectrometry. The phosphorus atoms diffuse into the Si substrate during the growth process. A P concentration of $10^{16} - 4 \times 10^{17}$ atoms/cm³ is measured in the top 300 nm of the Si. The gallium atoms do not diffuse far into the Si and the concentration drops below the detection limit ($\sim 10^{15}\text{cm}^{-3}$) within the first 20 nm. P atoms inside the Si crystal can be considered two-level systems (TLS) [21, 22] which are one of the main limitations for the quality factor of resonators [23] and the coherence times of superconducting qubits [24].

To investigate the loss due to the P doping, we fabricated test resonators on the Si substrate after removing the III-V layers and further etching into the Si substrate (see Appendix B for further details). The extracted internal quality factor Q_i as a function of the mean photon

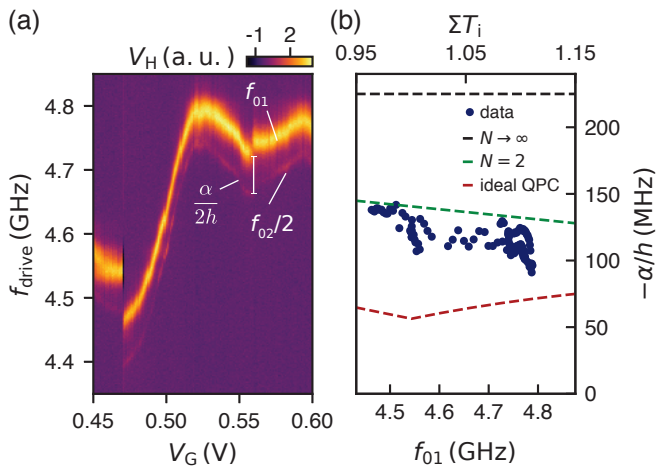


FIG. 2. **Qubit anharmonicity.** (a) Resonator response V_H as a function of gate top gate voltage V_G and drive frequency f_{drive} . The qubit is driven through the gate line with microwave pulses with a relatively high power P_{rf} on-chip such that the $|0\rangle \rightarrow |1\rangle$ with frequency f_{01} and the $|0\rangle \rightarrow |2\rangle$ with frequency $f_{02}/2$ are measured. (b). Extracted anharmonicity $-\alpha/h$ as a function of qubit frequency f_{01} and $\Sigma T_i = (hf_{01})^2/(2\Delta E_C)$. Dashed lines indicate model prediction for an ideal QPC (red), two channels with equal transmission (green) and the tunneling limit (black).

number $\langle n_{\text{ph}} \rangle$ for three different etch depths into the Si substrate is shown in the right panel of Fig. 1e. For an etch depth of 120 nm we find $Q_i < 10^4$ in the one photon regime. In contrast, we find $Q_i \approx 1 \times 10^5$ and $Q_i \approx 3 \times 10^5$ for etch depths 390 nm and 720 nm, respectively. The dielectric loss tangent associated with these quality factors is low enough to enable transmon devices with lifetimes of several microseconds where the exact limit depends on the qubit geometry due to the participation ratio of the electrical field at the surface and interfaces [13, 24, 25]. It should be noted that we measured $Q_i \approx 2 \times 10^5$ for a designated test resonator on the qubit device chip (Figs. 1a-b,d) after the entire fabrication.

IV. QUBIT SPECTROSCOPY

We next demonstrate gate control of the qubit device (Figs. 1a,b,d) and study the transport across the JJ using the qubit anharmonicity, for measurement details see Appendix C. Figure 2a shows a two-tone spectroscopy measurement of the qubit, where we measured the resonator response V_H as a function of gate voltage V_G and drive frequency f_{drive} . Due to the relatively high on-chip drive power $P_{\text{rf}} \approx -95$ dBm both the $|0\rangle \rightarrow |1\rangle$ transition at frequency f_{01} and two-photon $|0\rangle \rightarrow |2\rangle$ transition at frequency $f_{02}/2$ are resolved. With decreasing V_G the overall qubit frequency decreases and exhibits a non-monotonic gate response that is typically observed for gatemon qubits [2, 4–6]. We attribute the jumps in f_{01} and $f_{02}/2$ to switches of the channel configuration in the nanowire.

The current-phase relation of a semiconductor-based JJ is non-sinusoidal and can be described with a set of channel transmission coefficients $\{T_i\}$ consisting of a few channels with high transmission eigenvalues [26–28]. As a consequence, the gatemon anharmonicity, $\alpha/h = 2(f_{02}/2 - f_{01})$, in a gatemon is typically lower than for a metallic transmon [6], where $\alpha \approx -E_C$ [17, 29]. Here, we analyze α following Ref. [6] to study the JJ transmission. We calculate $\{T_i\}$ for each value of gate voltage using $\Sigma T_i = (hf_{01})^2/(2\Delta E_C)$, where we use the measured $\Delta/e = 190 \mu\text{eV}$ (Ref. [11]) and $E_C/h = 225$ MHz from finite-element simulations on an intrinsic Si substrate. Assuming N transmitting channels with equal transmission probability, T , the model gives $\alpha = -E_C(1 - 3E_J/(\Delta N))$. Figure 2b shows the anharmonicity as a function of f_{01} and ΣT_i . The data lie between the predicted value for $N = 2$ channels and the ideal quantum point contact (QPC) model in which channels are filled in a step-like manner with at most one partially transmitting channel [30]. The data suggest that the transport in the observed gate range is dominated by 2 channels. Given equal transmission probabilities [6] this sets a lower bound $T_{\text{min}} > \Sigma T_i/2 \sim 0.48$ on the junction transparency. Similar studies on gatemons based on VLS InAs/Al nanowires with in-situ grown epitaxial Al (Ref. [6]), where $\alpha \approx 100 - 150$ MHz, report two or three channels with $T_{\text{min}} = 0.4 - 0.9$. This result is in good agreement with DC transport data obtained for a nominally identical material stack in Ref. [11], where we conclude a high junction transparency from measurements of the excess current and observed signatures of multiple Andreev reflections.

V. COHERENT OSCILLATIONS AND COHERENCE TIMES

Next, we demonstrate basic qubit control using time-domain manipulation. Figure 3a shows coherent Rabi oscillations with a fixed drive frequency $f_{\text{drive}} = f_q = 4.47$ GHz where the on-chip drive power P_{rf} and the length of the qubit drive pulse τ were varied. The lower panel of Fig. 3a shows the fit to the data at $P_{\text{drive}} = -89$ dBm, where the data are described by a damped sinusoid with a linear increase. This additional linear increase in V_H (Fig. 3b) could be the result of leakage to higher order states [31]. This leakage is expected as the Rabi frequency is similar to the anharmonicity $|\alpha|/h$. See Appendix C for further details.

Figure 4b shows Ramsey fringes measured by using two $R_X^{\pi/2}$ pulses separated by a delay τ . The lower panel of the figure shows a fit of a damped sinusoid to a linecut of the data. From the fit we extract a dephasing time $T_2^* \approx 15$ ns. The extracted value is in good agreement with estimates of T_2^* from a fit to the power dependence of the qubit linewidth in spectroscopy as described in Ref. [32] (see Appendix D).

Figure 4a shows the pulse sequences that we use to

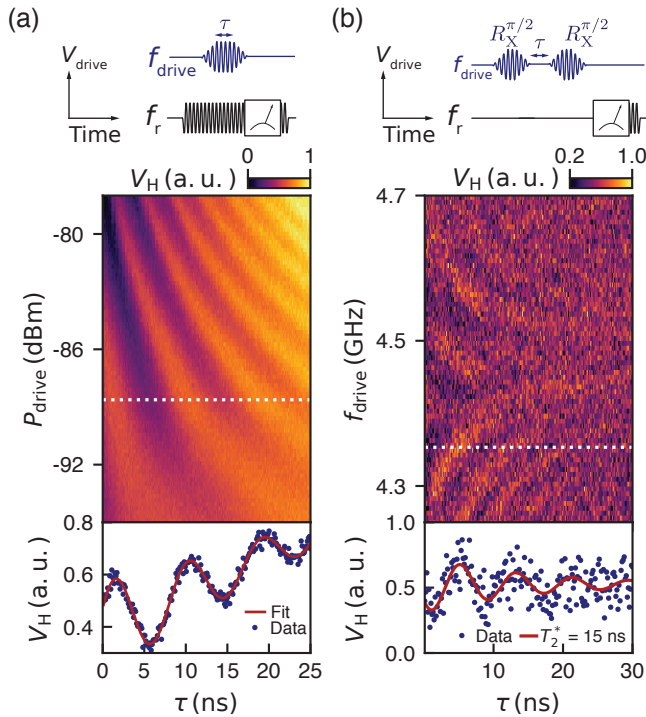


FIG. 3. **Coherent oscillations.** (a) The main panel shows Rabi oscillations as a function of drive power on-chip P_{drive} and pulse length τ at fixed drive frequency $f_{\text{drive}} = 4.47$ GHz. The pulse sequence used is shown above the plot. The lower panel shows a line cut at $P_{\text{drive}} = -89$ dBm (white dotted line) from the main panel. The solid line is a fit to the data using a damped sinusoid with a linear contribution. (b) The main panel shows Ramsey fringes as function of delay τ between $R_X^{\pi/2}$ pulses and f_{drive} . The pulse sequence is shown above. The lower panel shows a line cut at $f_{\text{drive}} = 4.205$ GHz (white dotted line) with a fit to a damped oscillation yielding $T_2^* \approx 15$ ns

measure the qubit lifetimes. We use overlapping drive and readout pulses to increase the signal-to-noise-ratio as the T_2^* time is shorter than the ring-up time of the readout resonator $\tau_{\text{rise}} \approx 480$ ns (see Appendix C). Figure 4b shows representative measurements of T_1 (red) and $T_{2,\text{echo}}$ (green) using a Hahn echo sequence with fits to an exponential decay.

Figure 4c shows the measured lifetimes for qubit frequencies between 3.5 and 5.0 GHz. T_1 and $T_{2,\text{echo}}$ are obtained from calibrated pulses and T_2^* is estimated from the qubit linewidth (Appendix D). The extracted mean values are $\bar{T}_1 = (740 \pm 110)$ ns, $\bar{T}_2^* = (21 \pm 7)$ ns, and $\bar{T}_{2,\text{echo}} = (1340 \pm 230)$ ns. The \bar{T}_1 and $\bar{T}_{2,\text{echo}}$ times are comparable with the lifetimes extracted for the first gatemon fabricated with VLS nanowires on a Si substrate [2]. However, an order of magnitude longer $T_2^* \approx 900$ ns were reported for those devices [2, 12].

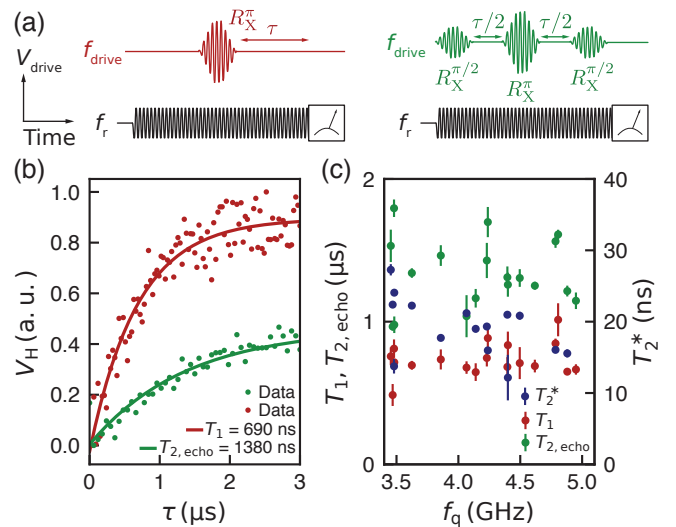


FIG. 4. **Qubit lifetimes.** (a) Pulse sequence for lifetime measurements. (b) T_1 and $T_{2,\text{echo}}$ measurement of the qubit at $f_q \approx 4.48$ GHz. (c) Lifetimes as a function of f_q . T_1 and $T_{2,\text{echo}}$ were measured with the pulse sequence shown in (a). T_2^* was extracted from the power dependence of the linewidth of the qubit in spectroscopy (Appendix D).

VI. DISCUSSION AND CONCLUSIONS

The measured dephasing times indicate that dephasing is limited by low-frequency noise since $T_{2,\text{echo}} \gg T_2^*$. We suspect that both the gate dielectric and dielectric close to the junction used for the selective area growth [11] cause the low decoherence times. Comparing previous Al-InAs based gatemon architectures, VLS-nanowire gatemons [2, 12] reported longer dephasing times ($T_{2,\text{VLS}}^* \approx 0.9 - 3.7$ μs) than gatemons based on 2DEGs [4] ($T_{2,2\text{DEG}}^* \approx 400$ ns) which are longer than the dephasing times in this work ($T_{2,\text{SAG}}^* \approx 20$ ns). For the VLS-nanowire gatemon the nanowire was placed on the device chip without additional dielectrics near the active junction region. In case of the 2DEG-gatemon, mesa material below the proximitized InAs channel and gate dielectric were still present near the junction on the qubit chip after device fabrication. Further, the mesa with a width of ~ 1 μm was smaller than the mesa in this work (~ 10 μm). The main difference in this work is the presence of residual growth dielectric with a low quality near the junction. The SiO_x layer in particular was optimized to have a low crystal quality to increase the selectivity of the InAs growth [10]. We expect this layer to have an increased TLS density compared to the mesa material and thus limit T_2^* .

The relaxation times of the qubits are lower than the relaxation times of the test resonator, indicating that T_1 is not limited by the dielectric loss of the substrate. Based on the internal quality factor measured for readout resonators $Q_i = 2 \times 10^5$, we would expect a relaxation time for a qubit with frequency $f_q = 5$ GHz of $T_1 \approx Q_i / (2\pi f_q) \approx 6$ μs . Instead the qubit could be lim-

ited by dielectric loss due to the III-V material or doped Si in the mesa region. Although we do not expect that the doping level is high enough for the doped Si to be conducting, we cannot exclude the possibility that normal conducting channels exist near the GaP/Si interface.

To improve T_2^* , the material quality near the junction needs to be improved. Further, the qubit can be better decoupled from the mesa by means of device design which leads to a reduced participation ratio [13, 25, 33] and, therefore, increased relaxation times. Potential changes in device fabrication and design are summarized in Appendix F. Other potential sources of decoherence such as gate noise and readout are discussed in Appendix G.

In summary, we have demonstrated that selective-area-grown Al-InAs nanowires on a Si substrate are a potential platform for voltage controlled transmon qubits. We implemented the SAG based gatemon on a low-loss substrate with relaxation times of roughly 700 ns and dephasing times of 20 ns. With further improvement of coherence this material platform opens new possibilities for scalable highly integrated quantum circuits such as gatemons [2], protected qubits [8], voltage-tunable quantum buses [34] and voltage-tunable quantum memories [35].

ACKNOWLEDGMENTS

We thank Anna Mukhortova for help with the process development. This work was supported by the Microsoft Corporation, the Danish National Research Foundation and VILLUM FONDEN.

Appendix A: Qubit device fabrication

The qubit devices were fabricated using a combination of standard electron-beam lithography and UV lithography. At the beginning of the qubit fabrication, the entire chip was covered with a 40 nm thick Al film on top of the dielectric layers consisting of 10 nm thick SiO_x and 5 nm thick AlO_x . In a first step, Al was etched selectively on the device chips using Al Etchant Transene D, only leaving Al in dumbbell-shaped areas around nanowires (Fig. 1b). Using the same resist stack, both SiO_x and AlO_x were etched using buffered HF solution. The dumbbell shape offers a compromise between little dielectric and Al being left around the nanowire [see Fig. 1b] and sufficiently large MBE Al patches with an area of $\sim 1 \mu\text{m}^2$ that are used to connect the Al-InAs nanowires to the rest of the circuit. Next, the mesa was defined by protecting the nanowire and a small surrounding area with photoresist (AZ5214E) while removing GaAs, GaP and ~ 400 nm of Si using two reactive ion etching steps. First, an etch with process gases Cl_2 and Ar was used that created an almost vertical mesa profile. The second etch, which used process gases Cl_2 and N_2 , created a trapezoidal mesa profile (see Fig. 1d). The first step was optimized to etch the material stack fast, reducing

heat load of the resist during the process, and creating steep side walls. The second step creates a trapezoidal shape, which is beneficial for the crawl up of top gate metal. Then, the JJ was defined by selectively removing a ~ 150 nm long Al segment on the nanowire using Transene Al Etchant Type D at 50°C . Next, Al for the readout circuit and qubit island definition was evaporated with a lift-off process, where the mesas were protected by resist. The evaporation was preceded by a 10 s long dip in buffered HF solution to remove surface oxides from the chip. The transmission line, readout resonators, qubit islands, a test resonator and gate lines were defined by selectively removing Al with a wet-etch solution (Transene Al Etchant Type D at 50°C). Next, 15 nm HfO_2 was grown by atomic layer deposition in lithographically pre-defined regions on top of the JJs. Additionally HfO_2 was deposited in areas where Al would climb mesas to ensure they were isolated. In these climbing areas PMMA bridges were defined by crosslinking PMMA through the exposure with 30 times the area dose that is typically used to pattern the resist (see Fig. 1d). Next, gates (200 nm thick Al) were evaporated. These were later used to tune the critical currents of the single JJs and thereby the qubit frequencies. In addition, Al wires leading from the nanowire to qubit islands and nanowire to the ground plane were deposited. In the final step, the nanowire, qubit island and ground plane were electrically connected by creating ohmic contacts. To ensure a good contact AlO_x on the Al wires and MBE Al was removed by Ar-milling prior to the deposition of a ~ 250 nm thick Al layer.

Appendix B: Resonator fabrication and measurements

Al test resonators were fabricated on the Si substrate after removing the entire GaAs and GaP buffer and deep etching into the Si substrate using the RIE steps described above. We also added patterned structures on the chip to measure the etch depth with a mechanical profilometer. The resonators were then defined by a global electron beam evaporation of 100 nm thick Al under high vacuum and subsequent selective etching of the Al using standard electron e-beam lithography and wet-etch techniques. Preceding the Al deposition, the device chip was dipped into buffered HF solution to remove surface oxides from the Si substrate.

For the extraction of the internal and external quality factors, Q_i and Q_{ext} , we used the fit procedure described in Ref. [36]. Fig. 5 shows an example fit in the few photon regime for a resonator made after etching the III-V layers and 720 nm of Si. Here, we used resonators for which $Q_{\text{ext}} \approx Q_i$ in the few photon regime. The data shown in Fig. 5 was taken at $P_{\text{on-chip}} = -149$ dBm, which corresponds to a mean photon number on chip of $\langle n_{\text{ph}} \rangle \approx 1$. The resonance frequency f_r of the resonator is at $f_r = 5.51$ GHz. From the fit we extracted

| Sample | Etch depth (nm) | f_r (GHz) | Q_{ext} (10^3) | Q_i (10^3) |
|--------|-----------------|-------------|-----------------------------|------------------|
| 1 | 120 | 6.35 | 12 | 27 |
| 2 | 390 | 5.46 | 20 | 102 |
| 3 | 720 | 5.51 | 57 | 371 |

TABLE I. Three resonator devices fabricated on Si with different etching parameters and their extracted resonance frequency f_r , external quality factor Q_{ext} and internal quality factor Q_i .

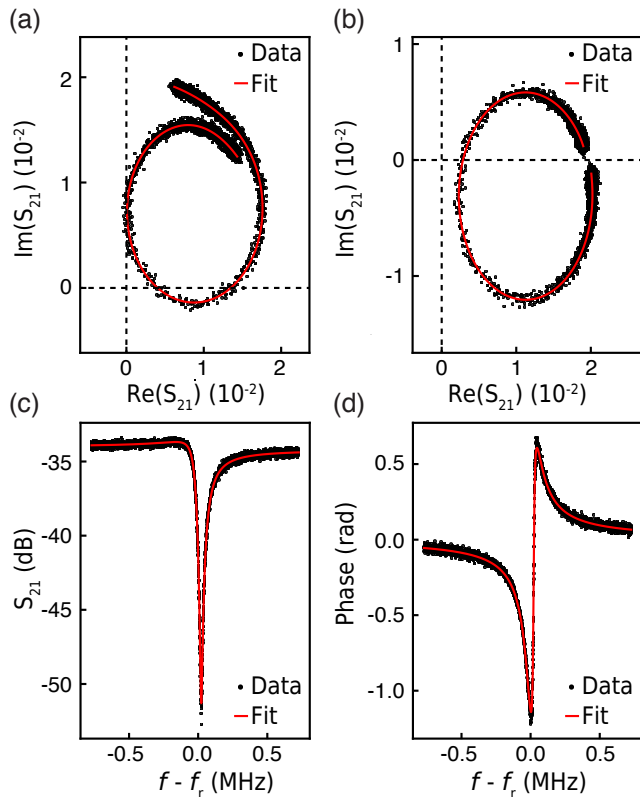


FIG. 5. Example data and fit of the resonator with an etch depth of 720 nm (see Fig. 1) at $P_{\text{on-chip}} = -149$ dBm. (a) Raw data (black) and fit (red) of the trajectory of S_{21} in the complex plane. (b) S_{21} data and fit after correcting for the cable delay [36, 37]. (c) and (d) show the magnitude and phase of S_{21} of the data in (a) with the corresponding fits.

$Q_i \approx 3.6 \times 10^5$ and $Q_{\text{ext}} \approx 57 \times 10^3$. We note, that for extracting Q_i , we use resonators for which the external quality factor Q_{ext} matches Q_i ($Q_{\text{ext}} \approx Q_i$) in the few photon regime.

We measured three resonator devices with different etch times. The results are summarized in Tab. I. The quality factor for device 1 was extracted from a fit at $P_{\text{on-chip}} = -125$ dBm, for device 2 at $P_{\text{on-chip}} = -146$ dBm and for device 3 at $P_{\text{on-chip}} = -148$ dBm.

Appendix C: Pulsed qubit measurements

All measurements in this work were performed with the qubit in the transmon limit ($E_J \gg E_C$) and in the dispersive regime $|f_q - f_r| \gg g/2\pi$, where $g/2\pi \approx 80$ MHz is the coupling between cavity and qubit island. In all experiments, the DC gate voltage V_G and the RF drive tone for the qubit are combined using a bias tee at the millikelvin stage of the dilution refrigerator and applied through the gate line.

We extracted the frequencies $f_{02}/2$ and f_{01} (Fig. 2a) by numerically fitting two independent Lorentzian line shapes to the signal and using the position of peak maxima as transition frequencies. For all qubit measurements in this work, the pulse length τ corresponds to the length of the plateau of a Gaussian flat top pulse with a rise time of $2\sigma = 4$ ns. All measurements in this work were limited to pulse lengths of ~ 30 ns due to the short dephasing time (see Section V). To increase signal-to-noise ratio and adjust for short qubit dephasing times as well as a low coupling between resonator and transmission line ($Q_c \approx 2 \times 10^4$), the resonator was driven during the qubit manipulation and resonator readout (pulse sequence shown in Figs. 3a) unless stated otherwise. Here, we estimate that the signal rise time of the resonator with $f_{\text{res}} \approx 6$ GHz is $\tau_{\text{rise}} \approx Q_c/2\pi f_{\text{res}} \sim 480$ ns. A non-overlapping pulse sequence in which the resonator drive was applied when the signal integration started was used to measure the data in Fig. 3b (Ramsey fringes). Measurements as shown in Fig. 3a were used to calibrate R_X^π and $R_X^{\pi/2}$ pulses that rotate the qubit state around the x -axis by π and $\pi/2$.

We note that for our qubit the T_2^* time (≈ 15 ns) is shorter than the ring-up time of the readout resonator (≈ 480 ns) and comparable to the minimum gate time to avoid state leakage, $\sim 1/(|\alpha|/h)$. In a standard measurement sequence including a π -pulse (see Figs. 6c and d) this could lead to leakage to higher order states. When driving we observe an additional slow oscillation in V_H (not shown) that we attribute to driving chip modes that are coupled to the qubit. The observed linear increase could be the onset of this slow oscillation. To test if the relaxation times are limited by leakage to higher order state we performed additional weak spectroscopy measurements. For these we used a weak spectroscopy pulse as drive tone as shown in Figs. 6a and b. Here, a low readout power was used to avoid an ac-Stark shift of the qubit caused by a high photon population in the resonator. Fig. 6e compares the relaxation times extracted from the different datasets and their respective exponential fit as illustrated in Fig. 6a-d. The pulsed measurement results (Figs. 6c-d), are in good agreement with the weak drive measurements.

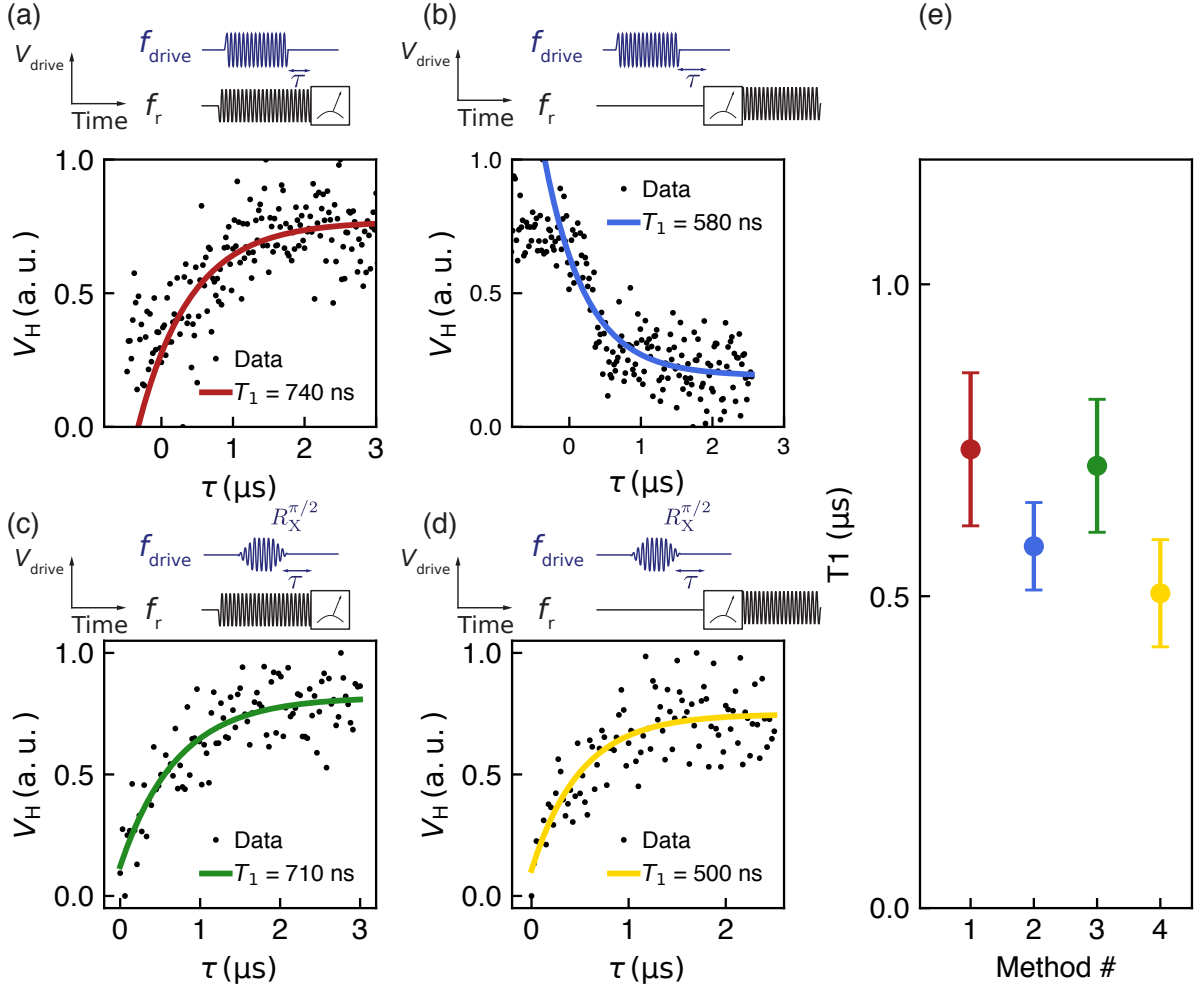


FIG. 6. **Different measurement methods for extraction of relaxation time T_1 .** (a) Readout and weak spectroscopy drive tone overlap. (b) The strong readout tone is applied after the spectroscopy drive tone. (c) A π -pulse is used to excite the qubit. This drive tone overlaps with the readout tone. (d) The readout tone is applied after π -pulse. (e) Comparison of extracted T_1 values from datasets (a)-(d).

Appendix D: Continuous drive T_2^* measurement

To estimate the dephasing time of the qubit, we follow the method described in Ref. [32]. Here, the linewidth of the qubit in spectroscopy can be described by the equation $2\pi\delta_{\text{HWHM}} = 1/T_2' = (1/T_2^{*2} + n_s w_{\text{vac}}^2 T_1/T_2^*)^{1/2}$, where δ_{HWHM} is the half width at half maximum of the spectroscopy feature, T_2' is the dephasing time, and $n_s w_{\text{vac}}^2$ is proportional to the drive power on-chip $P_{\text{drive},s}$ with $P_{\text{drive},s} = P_{\text{drive}} - 60\text{dB}$ (60dB accounts for cryogenic attenuators, line attenuation and filtering as depicted in Fig. 9) and T_2^* is the dephasing time at zero drive power. Figure 7a shows the spectroscopy signal as a function of $P_{\text{drive},s}$. At each value of $P_{\text{drive},s}$, we extract the linewidth by fitting to a Lorentzian line shape (Fig. 7b). As shown in Fig. 7c, T_2^* is extracted from a fit to the power dependence of the linewidth.

Appendix E: Gate voltage dependence

We performed T_1 measurements and spectroscopy sweeps to extract T_2^* from the line width at different gate voltages. In Fig. 8a we show the spectroscopy signal for gate voltages $-0.09\text{ V} < V_G < 0.3\text{ V}$. In this range $3.6\text{ GHz} < f_q(V_G) < 4.8\text{ GHz}$. In Figs. 8b, c the relaxation time T_1 and dephasing time T_2^* are shown for 20 different values of V_G and the qubit frequency $f_q(V_G)$ which we extracted from the spectroscopy data. Figure 8d shows T_1 and T_2^* as a function of gate dispersion df_q/dV_G calculated numerically from $f_q(V_G)$. As T_1 and T_2^* show no correlation with qubit frequency $f_q(V_G)$ we conclude that the qubit coherence times are not limited by gate noise.

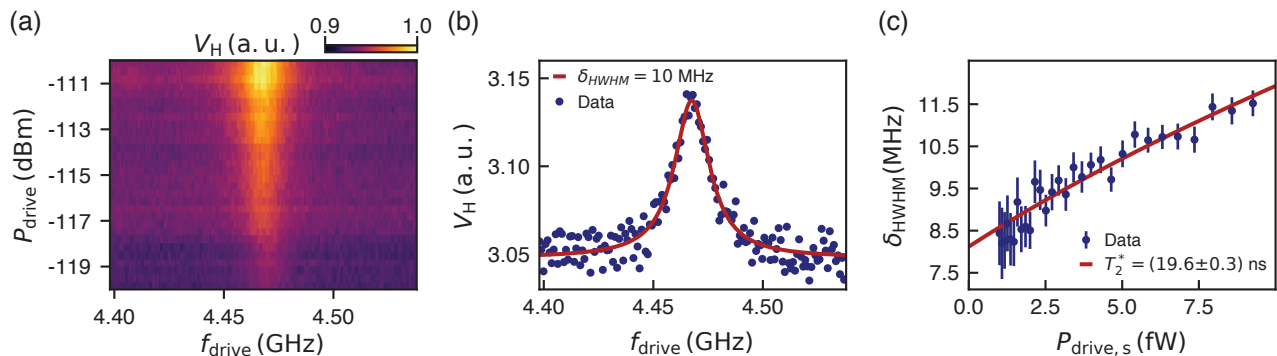


FIG. 7. **Spectroscopy data for estimation of dephasing time T_2^* .** (a) Spectroscopy signal as a function of qubit drive $P_{\text{drive},s}$ and drive frequency f_{drive} . (b) Linecut from (a) at $P_{\text{drive},s} = -116.7$ dBm with fit to Lorentzian lineshape (purple line). (c) Qubit linewidth δ_{HWHM} vs. power $P_{\text{drive},s}$ with fit using $2\pi\delta_{\text{HWHM}} = 1/T_2' = (1/T_2^{*2} + n_s w_{\text{vac}}^2 T_1/T_2^*)^{1/2}$. The decoherence time is estimated from the intersection of the fit with the y-axis.

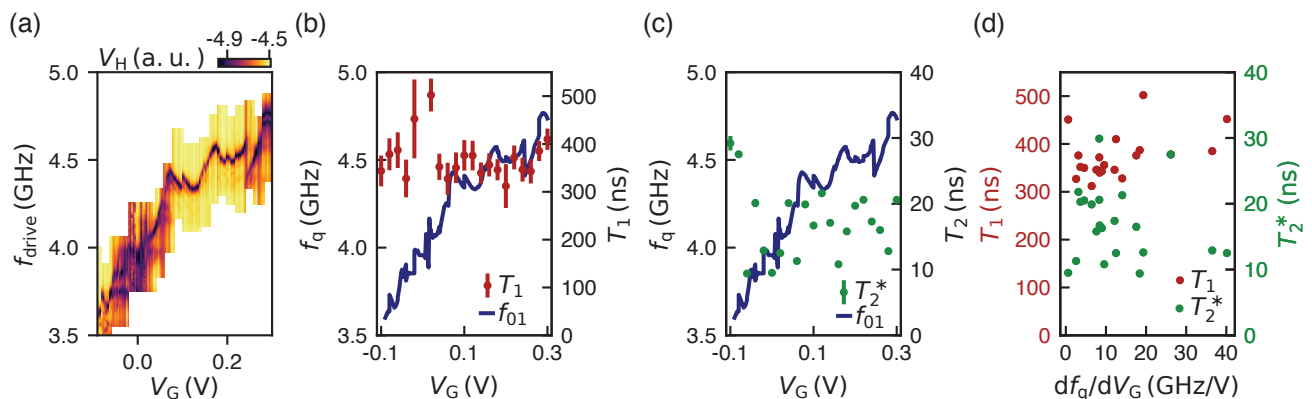


FIG. 8. **Coherence times and f_q as a function of V_G .** (a) Spectroscopy signal. (b) f_q as a function of V_G and T_1 for 20 different gate voltages. (c) Same as (b) but for T_2^* . (d) Coherence times T_1 and T_2^* as a function of gate dispersion df_q/dV_G .

Appendix F: Potential fabrication improvements

The mesa could be placed further away from strong electric fields generated by the qubit island and the mesa size could be reduced. This could be achieved by using a different dry etch chemistry. An isotropic wet etch could be used to create a concave mesa shape, leading to an increased distance and thus smaller coupling between the mesa and the residual circuit. A possible improvement for future devices is the definition of the mesa before the selective area growth, leading to a reduced mesa size, set by the diffusion length of particles during the MBE growth, and enabling the fabrication of the readout circuit and qubit island using MBE Al. Side gates could be used instead of top gates to remove gate dielectric from the process flow. The growth dielectric around nanowires could be removed by means of HF vapor etching or design changes. In order to decouple qubits from the lossy mesa stack, thicker PMMA bridges could be used.

Appendix G: Additional sources for decoherence

We can exclude setup related and measurement related dephasing mechanisms as limiting factors for the short dephasing times. Our system was calibrated with metallic fixed-frequency transmon devices, where $T_2^* \approx 10 \mu\text{s}$ was measured, and we used the same sample packaging as in Refs. [2, 4], where $T_2^* \approx 900$ ns and $T_2^* \approx 400$ ns were reported. Further, no correlation between the T_2^* and the gate dispersion df_q/dV_G is observed, indicating lifetimes are not limited by decay through the gate line or gate noise (Appendix E). Here we note that the Rabi frequencies in these measurements are comparable to the qubit anharmonicity $|\alpha|/h \sim 120$ MHz, potentially leading to leakage to higher order states and inducing dephasing [31]. To reduce the potential impact of this effect, Gaussian flat-top pulses were used to avoid driving higher order transition of the qubit system. To avoid additional dephasing due to photon number fluctuations we chose a low cavity readout power. Further, we confirmed that this overlapping pulse sequence yields the same lifetimes as alternative measurement techniques where we used non-overlapping pulses or prepared the qubit in a well-

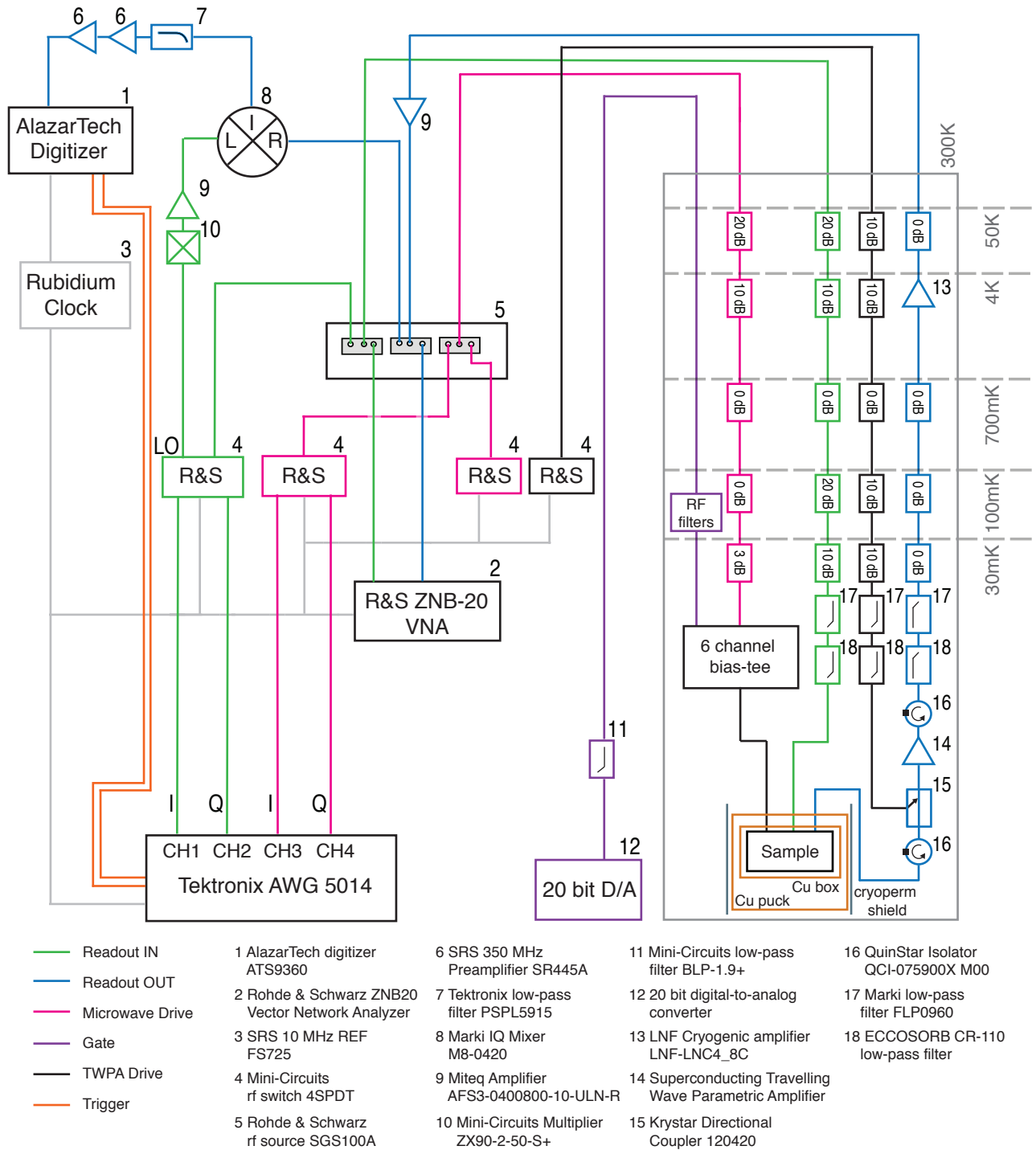


FIG. 9. **Schematic of the experimental setup used for the experiments.** The readout resonator can be driven by a vector network analyzer (VNA) or by a signal from a rf source that is modulated by an arbitrary waveform generator (AWG) (blue line). The amplified output signal can be read out either by the VNA or undergo down conversion by mixing with a reference signal. Microwave equipment is synchronized using a 10MHz clock reference. To tune the chemical potential of the SAG nanowire junction, a DC line (purple) is connected to the sample. The DC signal merges with the (pink) RF signal used for driving the qubit in a bias tee channel.

defined mixed state using long and weak spectroscopy pulses [38] (see Appendix C).

Appendix H: Setup

The presented measurements were acquired in a cryo-free dilution refrigerator with a base temperature of \sim

30mK. Fig. 9 shows a detailed schematic of the experimental setup. An RF switch is used to route signals to the sample that are either coming from the vector network analyzer (VNA) or from AWG modulated rf sources. The input signals are attenuated and filtered before reaching the sample. For measurements the RF switch can direct the readout signal back to the VNA or to the demodulation circuit. The latter consists of a mixer for down conversion of the output signal to an

intermediate frequency by mixing it with a reference tone. The signal is then filtered and amplified before it is finally digitized and digitally downconverted with the AlazarTech Digitizer. The microwave drive tone is generated by an additional R&S microwave source and is applied via its own drive line that merges with the gate line in a bias tee before reaching the sample. For synchronisation of all instruments an SR FS725 10 MHz clock reference is used.

-
- [1] F. Arute, K. Arya, R. Babbush, D. Bacon, J. C. Bardin, R. Barends, R. Biswas, S. Boixo, F. G. S. L. Brandao, D. A. Buell, B. Burkett, Y. Chen, Z. Chen, B. Chiaro, R. Collins, W. Courtney, A. Dunsworth, E. Farhi, B. Foxen, A. Fowler, C. Gidney, M. Giustina, R. Graff, K. Guerin, S. Habegger, M. P. Harrigan, M. J. Hartmann, A. Ho, M. Hoffmann, T. Huang, T. S. Humble, S. V. Isakov, E. Jeffrey, Z. Jiang, D. Kafri, K. Kechedzhi, J. Kelly, P. V. Klimov, S. Knysh, A. Korotkov, F. Kostritsa, D. Landhuis, M. Lindmark, E. Lucero, D. Lyakh, S. Mandrá, J. R. McClean, M. McEwen, A. Megrant, X. Mi, K. Michielsen, M. Mohseni, J. Mutus, O. Naaman, M. Neeley, C. Neill, M. Y. Niu, E. Ostby, A. Petukhov, J. C. Platt, C. Quintana, E. G. Rieffel, P. Roushan, N. C. Rubin, D. Sank, K. J. Satzinger, V. Smelyanskiy, K. J. Sung, M. D. Trevithick, A. Vainsencher, B. Villalonga, T. White, Z. J. Yao, P. Yeh, A. Zalcman, H. Neven, and J. M. Martinis, Quantum supremacy using a programmable superconducting processor, *Nature* **574**, 505 (2019).
- [2] T. W. Larsen, K. D. Petersson, F. Kuemmeth, T. S. Jespersen, P. Krogstrup, J. Nygård, and C. M. Marcus, Semiconductor-Nanowire-Based Superconducting Qubit, *Phys. Rev. Lett.* **115**, 127001 (2015).
- [3] G. de Lange, B. van Heck, A. Bruno, D. J. van Woerkom, A. Geresdi, S. R. Plissard, E. P. A. M. Bakkers, A. R. Akhmerov, and L. DiCarlo, Realization of microwave quantum circuits using hybrid superconducting-semiconducting nanowire Josephson elements, *Phys. Rev. Lett.* **115**, 127002 (2015).
- [4] L. Casparis, M. R. Connolly, M. Kjaergaard, N. J. Pearson, A. Kringhøj, T. W. Larsen, F. Kuemmeth, T. Wang, C. Thomas, S. Gronin, G. C. Gardner, M. J. Manfra, C. M. Marcus, and K. D. Petersson, Superconducting gatemon qubit based on a proximitized two-dimensional electron gas, *Nat. Nanotechnol.* **13**, 915 (2018).
- [5] J. I.-J. Wang, D. Rodan-Legrain, L. Bretheau, D. L. Campbell, B. Kannan, D. Kim, M. Kjaergaard, P. Krantz, G. O. Samach, F. Yan, J. L. Yoder, K. Watanabe, T. Taniguchi, T. P. Orlando, S. Gustavsson, P. Jarillo-Herrero, and W. D. Oliver, Coherent control of a hybrid superconducting circuit made with graphene-based van der Waals heterostructures, *Nat. Nanotechnol.* **14**, 120 (2019).
- [6] A. Kringhøj, L. Casparis, M. Hell, T. W. Larsen, F. Kuemmeth, M. Leijnse, K. Flensberg, P. Krogstrup, J. Nygård, K. D. Petersson, and C. M. Marcus, Anharmonicity of a superconducting qubit with a few-mode Josephson junction, *Phys. Rev. B* **97**, 060508(R) (2018).
- [7] A. Kringhøj, B. van Heck, T. W. Larsen, O. Erlandsson, D. Sabonis, P. Krogstrup, L. Casparis, K. D. Petersson, and C. M. Marcus, Suppressed Charge Dispersion via Resonant Tunneling in a Single-Channel Transmon, *Phys. Rev. Lett.* **124**, 246803 (2020).
- [8] T. W. Larsen, M. E. Gershenson, L. Casparis, A. Kringhøj, N. J. Pearson, R. P. G. McNeil, F. Kuemmeth, P. Krogstrup, K. D. Petersson, and C. M. Marcus, Parity-protected superconductor-semiconductor qubit, *Phys. Rev. Lett.* **125**, 056801 (2020).
- [9] S. J. Pauka, K. Das, R. Kalra, A. Moini, Y. Yang, M. Trainer, A. Bousquet, C. Cantaloube, N. Dick, G. C. Gardner, M. J. Manfra, and D. J. Reilly, A cryogenic cmos chip for generating control signals for multiple qubits, *Nature Electronics* **4**, 64 (2021).
- [10] F. Krizek, J. E. Sestoft, P. Aseev, S. Marti-Sanchez, S. Vaitiekėnas, L. Casparis, S. A. Khan, Y. Liu, T. c. v. Stankevič, A. M. Whiticar, A. Fursina, F. Boekhout, R. Koops, E. Uccelli, L. P. Kouwenhoven, C. M. Marcus, J. Arbiol, and P. Krogstrup, Field effect enhancement in buffered quantum nanowire networks, *Phys. Rev. Mater.* **2**, 093401 (2018).
- [11] A. Hertel, L. O. Andersen, D. M. T. van Zanten, M. Eichinger, P. Scarlino, S. Yadav, J. Karthik, S. Gronin, G. C. Gardner, M. J. Manfra, C. M. Marcus, and K. D. Petersson, Electrical Properties of Selective-Area-Grown Superconductor-Semiconductor Hybrid Structures on Silicon, *Phys. Rev. Appl.* **16**, 044015 (2021).
- [12] L. Casparis, T. W. Larsen, M. S. Olsen, F. Kuemmeth, P. Krogstrup, J. Nygård, K. D. Petersson, and C. M. Marcus, Gatemon Benchmarking and Two-Qubit Operations, *Phys. Rev. Lett.* **116**, 150505 (2016).
- [13] C. Wang, C. Axline, Y. Y. Gao, T. Brecht, Y. Chu, L. Frunzio, M. H. Devoret, and R. J. Schoelkopf, Surface participation and dielectric loss in superconducting qubits, *Appl. Phys. Lett.* **107**, 162601 (2015).
- [14] H. Toida, T. Nakajima, and S. Komiyama, Vacuum Rabi Splitting in a Semiconductor Circuit QED System, *Phys. Rev. Lett.* **110**, 066802 (2013).
- [15] M. Scigliuzzo, L. E. Bruhat, A. Bengtsson, J. J. Burnett, A. F. Roudsari, and P. Delsing, Phononic loss in superconducting resonators on piezoelectric substrates, *New J. Phys.* **22**, 053027 (2020).
- [16] J. O'Connell Yuan, K. S. Wickramasinghe, W. M. Strickland, M. C. Dartiaillh, K. Sardashti, M. Hatefipour, and J. Shabani, Epitaxial superconductor-semiconductor two-dimensional systems for superconducting quantum circuits, *J. Vac. Sci. Technol. A* **39**, 033407 (2021).

- [17] J. Koch, T. M. Yu, J. Gambetta, A. A. Houck, D. I. Schuster, J. Majer, A. Blais, M. H. Devoret, S. M. Girvin, and R. J. Schoelkopf, Charge-insensitive qubit design derived from the cooper pair box, *Phys. Rev. A* **76**, 042319 (2007).
- [18] G. C. Gardner, S. Fallahi, J. D. Watson, and M. J. Manfra, Modified MBE hardware and techniques and role of gallium purity for attainment of two dimensional electron gas mobility $> 35 \times 10^6 \text{cm}^2/\text{Vs}$ in AlGaAs/GaAs quantum wells grown by MBE, *J. Cryst. Growth* **441**, 71 (2016).
- [19] P. Krogstrup, N. L. B. Ziino, W. Chang, S. M. Albrecht, M. H. Madsen, E. Johnson, J. Nygård, C. M. Marcus, and T. S. Jespersen, Epitaxy of semiconductor–superconductor nanowires, *Nat. Mater.* **14**, 400 (2015).
- [20] W. Chang, S. M. Albrecht, T. S. Jespersen, F. Kuemmeth, P. Krogstrup, J. Nygård, and C. M. Marcus, Hard gap in epitaxial semiconductor–superconductor nanowires, *Nat. Nanotechnol.* **10**, 232 (2015).
- [21] P. W. Anderson, B. I. Halperin, and C. M. Varma, Anomalous low-temperature thermal properties of glasses and spin glasses, *Philos. Mag.* **25**, 1 (1972).
- [22] W. A. Phillips, Two-level states in glasses, *Rep. Prog. in Phys.* **50**, 1657 (1987).
- [23] J. Gao, M. Daal, A. Vayonakis, S. Kumar, J. Zmuidzinas, B. Sadoulet, B. A. Mazin, P. K. Day, and H. G. Leduc, Experimental evidence for a surface distribution of two-level systems in superconducting lithographed microwave resonators, *Appl. Phys. Lett.* **92**, 152505 (2008).
- [24] J. Lisenfeld, A. Bilmes, A. Megrant, R. Barends, J. Kelly, P. Klimov, G. Weiss, J. M. Martinis, and A. V. Ustinov, Electric field spectroscopy of material defects in transmon qubits, *NPJ Quantum Inf.* **5**, 105 (2019).
- [25] M. Sandberg, V. P. Adiga, M. Brink, C. Kurter, C. Murray, M. Hopstaken, J. Bruley, J. S. Orcutt, and H. Paik, Investigating microwave loss of SiGe using superconducting transmon qubits, *Appl. Phys. Lett.* **118**, 124001 (2021).
- [26] E. M. Spanton, M. Deng, S. Vaitiekėnas, P. Krogstrup, J. Nygård, C. M. Marcus, and K. A. Moler, Current-phase relations of few-mode InAs nanowire Josephson junctions, *Nat. Phys.* **13**, 1177 (2017).
- [27] M. F. Goffman, C. Urbina, H. Pothier, J. Nygård, C. M. Marcus, and P. Krogstrup, Conduction channels of an InAs-Al nanowire Josephson weak link, *New J. Phys.* **19**, 092002 (2017).
- [28] F. Nichele, E. Portolés, A. Fornieri, A. M. Whiticar, A. C. C. Drachmann, S. Gronin, T. Wang, G. C. Gardner, C. Thomas, A. T. Hatke, M. J. Manfra, and C. M. Marcus, Relating Andreev Bound States and Supercurrents in Hybrid Josephson Junctions, *Phys. Rev. Lett.* **124**, 226801 (2020).
- [29] P. Krantz, M. Kjaergaard, F. Yan, T. P. Orlando, S. Gustavsson, and W. D. Oliver, A quantum engineer’s guide to superconducting qubits, *Appl. Phys. Rev.* **6**, 021318 (2019).
- [30] C. W. J. Beenakker, Quantum transport in semiconductor-superconductor microjunctions, *Phys. Rev. B* **46**, 12841 (1992).
- [31] M. J. Peterer, S. J. Bader, X. Jin, F. Yan, A. Kamal, T. J. Gudmundsen, P. J. Leek, T. P. Orlando, W. D. Oliver, and S. Gustavsson, Coherence and Decay of Higher Energy Levels of a Superconducting Transmon Qubit, *Phys. Rev. Lett.* **114**, 010501 (2015).
- [32] D. I. Schuster, A. Wallraff, A. Blais, L. Frunzio, R.-S. Huang, J. Majer, S. M. Girvin, and R. J. Schoelkopf, ac Stark Shift and Dephasing of a Superconducting Qubit Strongly Coupled to a Cavity Field, *Phys. Rev. Lett.* **94**, 123602 (2005).
- [33] A. Bilmes, A. Megrant, P. Klimov, G. Weiss, J. M. Martinis, A. V. Ustinov, and J. Lisenfeld, Resolving the positions of defects in superconducting quantum bits, *Sci. Rep.* **10**, 3090 (2020).
- [34] L. Casparis, N. J. Pearson, A. Kringhøj, T. W. Larsen, F. Kuemmeth, J. Nygård, P. Krogstrup, K. D. Petersson, and C. M. Marcus, Voltage-controlled superconducting quantum bus, *Phys. Rev. B* **99**, 085434 (2019).
- [35] K. Sardashti, M. C. Dartiaill, J. Yuan, S. Hart, P. Gumann, and J. Shabani, Voltage-tunable superconducting resonators: A platform for random access quantum memory, *IEEE Transactions on Quantum Engineering* **1**, 1 (2020).
- [36] A. Bruno, G. De Lange, S. Asaad, K. Van Der Enden, N. Langford, and L. DiCarlo, Reducing intrinsic loss in superconducting resonators by surface treatment and deep etching of silicon substrates, *Appl. Phys. Lett.* **106**, 182601 (2015).
- [37] S. Probst, F. B. Song, P. A. Bushev, A. V. Ustinov, and M. Weides, Efficient and robust analysis of complex scattering data under noise in microwave resonators, *Rev. Sci. Instrum.* **86**, 024706 (2015).
- [38] M. Mergenthaler, A. Nersisyan, A. Patterson, M. Esposito, A. Baumgartner, C. Schönenberger, G. A. D. Briggs, E. A. Laird, and P. J. Leek, Circuit Quantum Electrodynamics with Carbon-Nanotube-Based Superconducting Quantum Circuits, *Phys. Rev. Appl.* **15**, 064050 (2021).